Simulation of the Dual-Frequency Radar Image of Asteroid 2016 HO3 and Implication for Tianwen-2 Mission

Niutao Liu, *Member, IEEE*, Ya-Qiu Jin, *Life Fellow, IEEE*, and Feng Xu, *Senior Member, IEEE*

***Abstract*—In China's Tianwen-2 mission, a dual-frequency radar will be carried out to detect the asteroid 2016 HO3. The dual-frequency radar can acquire the information of the asteroid's surface and internal structure. There are few studies about the radar detection of the asteroid 2016 HO3 and it is unclear what information can be acquired from the radar images. In this article, the radar images of the asteroid under nadir and oblique observations are simulated with the two-scale model of the Kirchhoff approximation/small-perturbation method. The radar images at 900 and 150 MHz are simulated to study the backscattering from the asteroid's surface and the detectability of the internal structure in the asteroid. The influences of the asteroid characteristics, such as the shape, surface roughness, internally embedded object, and the loss tangent of the media, on the radar images and the detectability of internal structure are discussed under nadir and oblique observations. The simulations provide a reference for future data analysis in the Tianwen-2 mission.**

***Index Terms*—Asteroid, imaging, radar, scattering, Tianwen-2.**

I. Introduction

TIANWEN-2 (Quest for Heavenly Truth-2) satellite, which is scheduled to launch in 2025, will carry a dual-frequency radar to detect the asteroid 2016 HO3 [1], [2], [3]. It might reveal the internal structure and composition of the asteroid for better understanding the formation of the asteroid.

The 2016 HO3 is a quasi-satellite of the Earth [4] whose orbit is in the neighborhood of the Earth–Moon system. Its diameter is approximately in the range of 30–90 m [5], and its spin rate is 0.47 h [6].

Space-borne and ground-based radars are widely used in detecting other planets and asteroids. Space-borne radars of the Moon, Venus, and Titan have been in operation for a long time [7], [8], [9], [10]. The lunar orbiting satellites Chandrayaan-2 and Lunar Reconnaissance Orbiter carried dual-frequency synthetic aperture radar to map the topography of the Moon [7], [8]. Ground-based radars are used to acquire the radar images of asteroids and estimate the shape of the asteroids [11], [12].

Manuscript received 2 July 2024; revised 13 August 2024; accepted 14 August 2024. Date of publication 16 August 2024; date of current version 5 September 2024. This work was supported by the National Natural Science Foundation of China under Grant 62201154. *(Corresponding author: Niutao Liu.)*

The authors are with the Key Laboratory of Information Science of Electromagnetic Waves (MoE), Fudan University, Shanghai 200433, China (e-mail: ntliu@fudan.edu.cn).

Digital Object Identifier 10.1109/JSTARS.2024.3445141

Because the asteroid 2016 HO3 is far away from the Tianwen-2 satellite, the radar beam can cover the whole asteroid, which is different from the previous observations of radars onboard rovers and satellites in Lunar and Mars detection missions [7], [8], [13], [14], [15], [16].

The center frequencies of the Tianwen-2 radar are 900 and 150 MHz [1], [2], [3]. The radar transmits circular polarization and receives both horizontally and vertically linear polarizations. The high-frequency radar can map the surface topography of the asteroid, while the low-frequency radar is able to detect the internal structure. The radar is in operation at the altitude of about 600 m hovering above the asteroid [1], [2], [3].

The backprojection method was used to produce the radar image of 2016 HO3 [3]. However, speckle noise is not included in the simulated radar image. In addition, the scatterings of rough surface and the internal structure were not considered. Many questions, such as what can be seen by dual-frequency radar, if the internal structures can be detected, and what are the main factors that will influence the radar image, remain to be answered.

The dielectric constants of the asteroid media, especially the loss tangent, will affect the penetration depth of the radar waves if the internal structure can be reached. In addition, the backscattering from rough surface may confuse the echoes directly from internal structure as well. To study the influences of these factors, 3-D ellipsoids with different shapes and spin axes are modeled for the simulation of radar images with and without internal scatterers [17], [18]. The speckle noise is included in simulated radar images. Based on the simulations, the influences of the loss tangent and internal structure of the asteroid are analyzed.

The rest of this article is organized as follows. Section II introduces the geometry of the asteroid, the backscattering model of the asteroid, and the radar imaging method. Section III presents the simulated radar image under nadir and oblique observations at dual frequencies. The low-frequency radar images of the asteroid with and without internal structure are analyzed. Section IV discusses the influence of surface roughness and loss tangent of the media. Finally, Section V concludes this article.

II. Method

A. Geometry of the Asteroid Model

Based on the light curve data, the asteroid 2016 HO3 is likely to be an ellipsoid [6]. The possible axis lengths are about

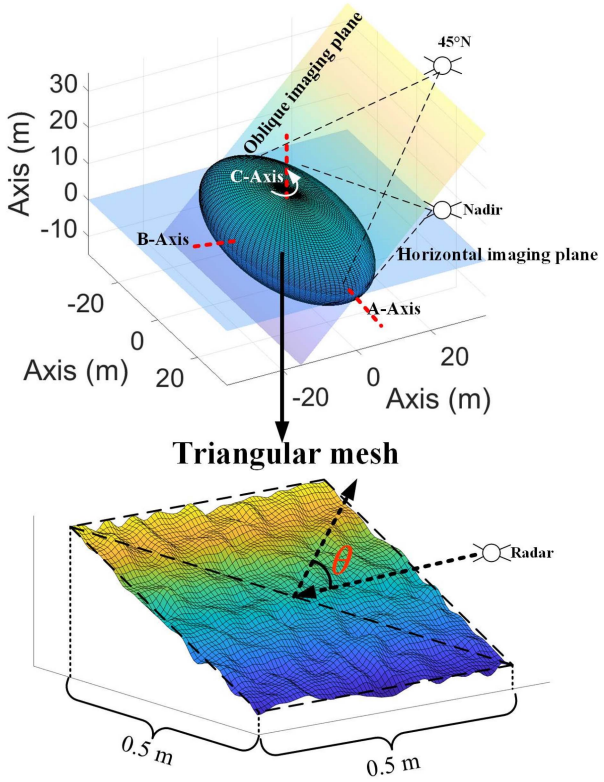

Fig. 1. Radar observation of the asteroid.

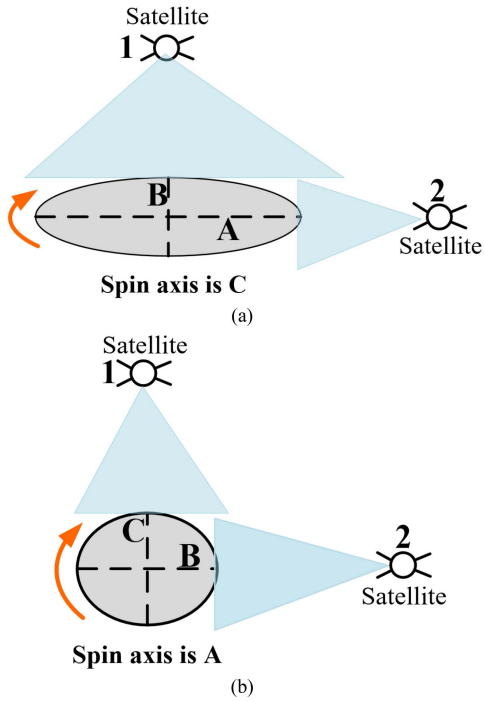

Fig. 2. Observation directions. (a) Spin axis is the shortest axis *C*. (b) Spin axis is the longest axis *A*.

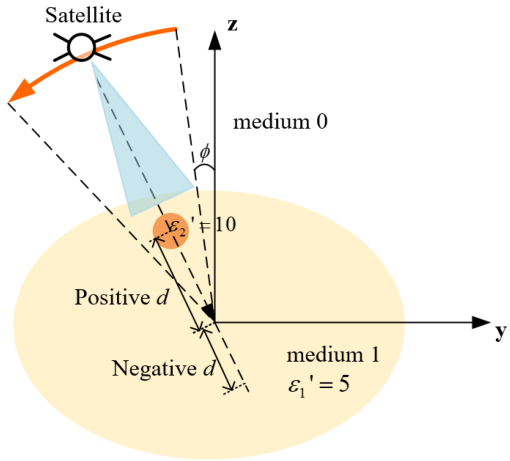

Fig. 3. Observation of internal sphere. The change of the observation position relative to the asteroid is the same as the satellite circles around the asteroid.

59 m × 28 m × 28 m, 66 m × 32 m × 22 m, and 89 m × 27 m × 19 m. Fig. 1 shows the asteroid model with axis lengths of $A \times B \times C$. The axis A is the longest axis, and the axis C is the shortest axis. The radar will observe the equator of the asteroid vertically and obliquely when hovering above the equator and at the latitude of 45°N/S [1], [2], [3]. The asteroid surface is numerically divided into small triangle meshes with a length of 0.5 m projected on the horizontal plane, as indicated in Fig. 1. Scatterings from roughness on each mesh are calculated by the two-scale model with the local incidence angle θ.

When the satellite hovers above the asteroid, as shown in Fig. 1, the radar can observe the rotating asteroid. The spin axis is the short C-axis in Fig. 1.

The radar images observed at positions 1 and 2 in Fig. 2 are simulated. The radar observes the asteroid parallel to the B-axis and A-axis at positions 1 and 2 in Fig. 2(a), and the spin axis is the C-axis. In Fig. 2(b), the radar observes the asteroid parallel to the C-axis and B-axis at positions 1 and 2 and the spin axis is the A-axis. When the spin axis is the B-axis, the observation is similar to Fig. 2(a), and the calculation is not repeated.

The satellite hovers about 600 m above the asteroid's surface. The center of the asteroid is supposed to be located at the coordinates (0, 0, 0). The distance between the radar and the center of the asteroid is assumed to be 625 m. As a heterogeneous body, a small dielectric spherical object with a diameter of 4 m is placed inside the asteroid on the line between the satellite and the center of the asteroid in Fig. 3. The sphere is numerically divided into small triangle meshes with a length of 0.5 m as well. It is assumed that the distance between the center of the sphere and ellipsoid is d. When the small sphere is closer to the radar than the center of ellipsoid, d is positive. Otherwise, d is negative. The rotation of the asteroid is equal to that the satellite rotates around the asteroid in opposite direction in Fig. 3.

Most of the asteroids are rocks with a dielectric constant ε' larger than 5 [19]. The loss tangents of lunar rocks are larger than 0.001 and can reach 0.1 [19]. In the simulation, it is assumed that ε' of the media 1 and 2 are 5 and 10, respectively.

B. Surface Scattering Model

The Tianwen-2 radar will transmit stepped-frequency waveform [3]. The backscattered signals at discrete frequencies can be received. The parameters, such as the pulsewidth and time

window, will be determined during flight, depending on the altitude of the orbit [2]. In the simulation, the signals at frequency domain are simulated. The information of pulsewidth and time window is unnecessary. The radar echoes at discrete frequency f_j and the observation angle ϕ_t, as shown in Fig. 3, can be calculated [20]

$$h_{pq}(f_j,\phi_t)=\sum_{n=1}^{N}S_{pq}^{n}\exp\left(-i4\pi\frac{R^n(\phi_t)}{c}f_j\right) \tag{1}$$

where R^n is the distance between the radar and the mesh n. N is the total number of mesh. c is the light speed in free space. The component S_{pq}^n of the scattering matrix of the mesh n relies on the area A_n and the reflectivity γ_{pq}^n of the mesh n [20], [21]

$$S_{pq}^{n}=\gamma_{pq}^{n}\sqrt{\frac{A_n}{4\pi}} \tag{2}$$

where the subscript q is the transmitted polarization and p is the received polarization.

The slopes of each mesh will rotate the local polarization base and change the local incidence angles. The relationship between the scattering matrix $\overline{\overline{\gamma}}$ in the principal reference system and the scattering matrix $\overline{\overline{\gamma}}'$ in the local coordinate system is [17], [20]

$$\overline{\overline{\gamma}}=\overline{\overline{U}}^{-1}(\psi)\cdot\overline{\overline{\gamma}}'\cdot\overline{\overline{U}}(\psi) \tag{3}$$

and

$$\overline{\overline{\gamma}}'(\theta)=\begin{bmatrix}a_{\mathrm{HH}}(\theta) & 0\\ 0 & a_{\mathrm{VV}}(\theta)\end{bmatrix}\cdot w(\theta) \tag{4}$$

where θ is the local incidence angle. The relative phase between $\gamma_{\mathrm{HH}}{}'$ and $\gamma_{\mathrm{VV}}{}'$ is assumed to be 0° for surface scattering. The rotation matrix $\overline{\overline{U}}(\psi)$ is [20]

$$\overline{\overline{U}}(\psi)=\begin{bmatrix}\cos\psi & \sin\psi\\ -\sin\psi & \cos\psi\end{bmatrix} \tag{5}$$

where ψ is the rotation angle of the polarization base.

When the local incidence angle is small, the quasi-specular scatterings dominate. Kirchhoff approximation (KA) is used under small incidence angles [22]

$$a_{pp}^{01}=\frac{\sqrt{\varepsilon_0}-\sqrt{\varepsilon_1}}{\sqrt{\varepsilon_0}+\sqrt{\varepsilon_1}} \tag{6}$$

$$\left\langle|w(\theta)|^2\right\rangle=\frac{1}{4\cos^4\theta\delta_1^2/L_1^2}\exp\left[-\frac{\tan^2\theta}{4\delta_1^2/L_1^2}\right] \tag{7}$$

where ε_0 and ε_1 are the relative permittivities of the vacuum and asteroid surface medium 1 in Fig. 3. The subscript pp corresponds to the horizontal (HH) or vertical (VV) polarization. L_1 is the correlation length of the large-scale roughness and δ_1 is the root-mean-square height. Here, it is assumed $\delta_1/L_1=0.08$.

When the incidence angle is large, diffuse scatterings from small-scale roughness can be calculated with the small-perturbation method (SPM) [22], [23]

$$a_{\mathrm{HH}}^{01}=\frac{\sqrt{\varepsilon_0}\cos\theta-\sqrt{\varepsilon_1-\varepsilon_0\sin^2\theta}}{\sqrt{\varepsilon_0}\cos\theta+\sqrt{\varepsilon_1-\varepsilon_0\sin^2\theta}} \tag{8}$$

$$a_{\mathrm{VV}}^{01}=(\varepsilon_1-\varepsilon_0)\frac{\varepsilon_0\sin^2\theta-\varepsilon_1(1+\sin^2\theta)}{\left[\varepsilon_1\cos\theta+(\varepsilon_1-\varepsilon_0\sin^2\theta)^{1/2}\right]^2} \tag{9}$$

$$\left\langle|w(\theta)|^2\right\rangle=4k^4\delta_2^2\cos^4\theta L_2^2\exp\left[-(kL_2\sin\theta)^2\right] \tag{10}$$

where $w(\theta)$ is a complex variable whose real part and imagery part are independent Gaussian random variables with zero mean [24]. k is the wavenumber in vacuum. L_2 is the correlation length of the small-scale roughness and δ_2 is the root-mean-square height. For SPM, it is assumed that $L_2=3/k$ and $\delta_2=0.3/k$. The correlation length and root-mean-square height were validated with the Chandrayaan-2 synthetic aperture radar data [20]. At small incidence angles, $\langle|\gamma'_{pq}|^2\rangle$ of KA is larger than that of SPM and the scattering coefficients of KA are utilized. While at large incidence angles, SPM is used. There are uncertainties in the roughness because the roughness of asteroid is unknown. The influence of roughness on scatterings will be discussed. The relative dielectric constant of asteroid surface medium is assumed to be 5, which is in the range of the measured values of lunar samples [19].

C. Internal Scattering Model

For low-frequency radar, the scatterings from the internal structure at discrete frequency f_j and the observation angle ϕ_t can be written as follows:

$$h_{pq}^{\mathrm{in}}(f_j,\phi_t)=\sum_{n=1}^{N_{\mathrm{in}}}T_{pq}A_t^nS_{pq}^n\exp\left(-i4\pi\left(\frac{R_{\mathrm{out}}^n(\phi_t)}{c}+\frac{R_{\mathrm{in}}^n(\phi_t)}{v}\right)f_j\right) \tag{11}$$

where T_{pq} is the transmission coefficient. N_{in} is the total number of the mesh of the internal structure. When calculating T_{pq}, the surface of the asteroid is taken as a flat and smooth plane. Fresnel transmission coefficient is used. The small sphere embedded in the asteroid is divided into small triangle meshes with a length of 0.5 m as well. The surface scattering component S_{pq}^n of the small sphere in the asteroid can be calculated with the two-scale rough surface model in (2)–(10) by replacing the ε_0 and ε_1 with ε_1 and ε_2. R_{in}^n is the distance from mesh n of the small sphere in the asteroid to the surface of the asteroid. R_{out}^n is the distance from mesh n to the radar in the vacuum. $v=c/\sqrt{\varepsilon_1}$ is the speed of the radar wave in asteroid.

The attenuation coefficient is

$$A_t^n=\exp\left(-2\kappa_aR_{\mathrm{in}}^n(\phi)\right). \tag{12}$$

The attenuation coefficient mentioned below is $20\log_{10}(A_t)$ in unit of dB. The absorption coefficient κ_a of the amplitude of the electric field is [21]

$$\kappa_a=\frac{\pi f\sqrt{\varepsilon'}\tan\delta}{c}. \tag{13}$$

Here, the ratio of the imaginary part ε'' and real part ε' of the dielectric constant is defined as the loss tangent $\tan\delta$.

The scatterings from particles depend on the size of particles and the wavelength. For particles whose sizes are in the range

of lunar soils, the scatterings can be ignored compared with the surface scattering [23]. So, the volume scatterings from particles are not included here.

D. Imaging Method

When the asteroid spins, the radar can detect the asteroid from varied incidence angles. The change of the observation position relative to the asteroid is the same as the satellite circles around the asteroid in Fig. 3. The received echoes at discrete frequency f_j and the observation angle ϕ_t can be simulated. By applying the 2-D inverse Fourier transform to the simulated echoes, the radar image I_{pq} can be produced [25]. The Hamming window is applied to suppress sidelobes when producing the radar image. The range resolution r_g and azimuth resolution r_a are as follows [18]:

$$r_g = \frac{c}{2B_w} \tag{14a}$$

$$r_a = \frac{\lambda_0}{2\phi_w} \tag{14b}$$

where c is the speed of light in vacuum. B_w is the bandwidth. λ_0 is the center wavelength. ϕ_w is the span of the spin angle in Fig. 3.

For the high-frequency radar, the frequency ranges from 300 MHz to 1.5 GHz [1], [2], [3]. In simulation, the radar echoes from 825 to 975 MHz are simulated. The bandwidth is 150 MHz. The resolution in range direction is 1 m/pixel. The span angle ϕ_w of the observation is set to be 9.55°. The resolution in azimuth is 1 m/pixel as well.

For the low-frequency radar of Tianwen-2, the frequency is from 130 to 170 MHz [1], [2], [3]. The bandwidth is 40 MHz. In the simulation, the bandwidth is 40 MHz as well. The span angle ϕ_w is assumed to be 15.28°. The resolutions in range and azimuth are both 3.75 m/pixel.

To illustrate how the speckle noise is included in the simulation, the analytical expression of the responses of each pixel in radar image is derived. When the distance between the radar and target is large enough, the incident wave can be taken as plane wave. Equation (1) can be approximated as follows:

$$h_{pq}(f_j, \phi_t) = \sum_{n=1}^{N} S_{pq}^n \exp\left(-i4\pi \frac{f_j}{c} \widehat{k}_t \overline{R}_n\right) \tag{15}$$

where the unit vector of the incidence $\widehat{k}_t$ is

$$\widehat{k}_t = \sin\phi_t \widehat{y} - \cos\phi_t \widehat{z} \tag{16}$$

$\widehat{y}$ and $\widehat{z}$ are the unit vectors in Fig. 3. When the angle ϕ_t approaches 0°, there is $\sin\phi_t \approx \phi_t$ and $\cos\phi_t \approx 1$. The vector from the radar to the mesh n is

$$\overline{R}_n = R_0 \widehat{k}_t + \overline{r}_n \tag{17a}$$

$$\overline{r}_n = r_{xn}\widehat{x} + r_{yn}\widehat{y} + r_{zn}\widehat{z}. \tag{17b}$$

R_0 is the distance between the radar and the center of the asteroid. r_n is the vector from the center of the asteroid to the mesh n. By applying discrete inverse Fourier transformation to (15), the response of each pixel can be written as follows:

$$I_{pq}(m_p, n_p) = \frac{1}{M_p N_p} \sum_{j=0}^{M_p-1} \sum_{t=0}^{N_p-1} h_{pq}(f_j, \phi_t) \exp\left(\frac{i2\pi n_p}{N_p} t\right) \exp\left(\frac{i2\pi m_p}{M_p} j\right). \tag{18}$$

For meshes around the pixel (m_p, n_p) and for a narrow bandwidth, the response can be approximated as follows [25]:

$$\begin{aligned} I_{pq}(m_p, n_p) = \sum_{n=1}^{N} S_{pq}^n \exp\Big\{ & -\frac{i4\pi f_c}{c}\left(r_{yn}\phi_c - (r_{zn} - R_0)\right) \\ & + i\pi(m_p + n_p)\Big\} \\ & \cdot \operatorname{sinc}\left\{\pi\left[\frac{2B_w(r_{zn} - R_0)}{c} + m_p\right]\right\} \\ & \cdot \operatorname{sinc}\left[\pi\left(\frac{-2f_c r_{yn}\phi_w}{c} + n_p\right)\right]. \end{aligned} \tag{19}$$

Here, ϕ_c is the center observation angle and f_c is the center frequency. Speckle noise is caused by the coherent summation of the random scattering fields. The random scattering fields from each mesh are modeled with the complex Gaussian random variable $w(\theta)$. The simulated responses at each pixel are the summation of the random scattering fields from meshes around each pixel. So, the speckle noise is included in the simulation. The strong backscattering from meshes near the nadir point will enhance the amplitude of the responses in the neighboring pixels, resulting in cross bright spot.

With the simulation of full-polarized scattering components, the compact polarized components can be derived. Assuming that the radar transmits left-circular polarization, the received horizontal and vertical polarization can be written as follows [17], [18]:

$$I_{\mathrm{HL}} = \left(-iI_{\mathrm{HH}} + I_{\mathrm{HV}}\right)/\sqrt{2} \tag{20a}$$

$$I_{\mathrm{VL}} = \left(-iI_{\mathrm{VH}} + I_{\mathrm{VV}}\right)/\sqrt{2}. \tag{20b}$$

The first Stokes parameter, which is the total backscattering power, can be written as follows [17]:

$$S_1 = \left\langle |I_{\mathrm{HL}}|^2 + |I_{\mathrm{VL}}|^2 \right\rangle. \tag{21}$$

All the radar images simulated in this article are $10\log_{10}(S_1)$ data.

III. Results

A. Nadir Observation at 900 MHz

The penetration depth of radar can be written as follows:

$$d_p = \frac{c}{2\pi f \tan\delta\sqrt{\varepsilon'}}. \tag{22}$$

The penetration depth at 900 MHz is 0.2 m when the loss tangent of medium 1 is as high as 0.1. The small penetration depth may exclude the scatterings from embedded objects. At 900 MHz, the scatterings from embedded objects are not included.

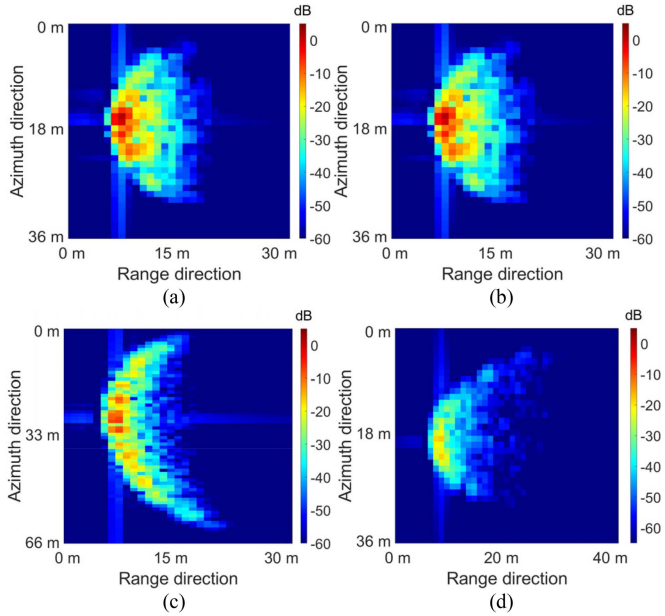

Fig. 4. Radar images of the asteroid with size of 59 m × 28 m × 28 m under nadir observation at 900 MHz. r_g and r_a are both 1 m/pixel. (a) Radar is at position 1. (b) Radar is at position 2. The spin axis of (a) and (b) is *A*. (c) Radar is at position 1. (d) Radar is at position 2. The spin axis of (c) and (d) is *C*.

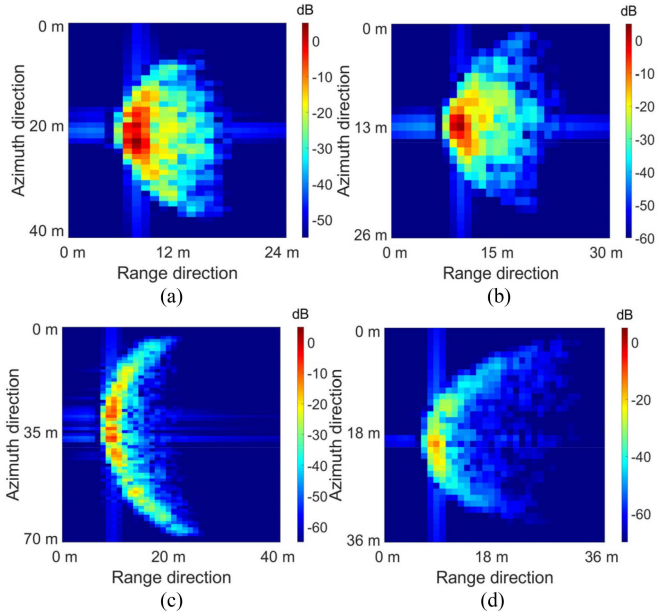

Fig. 5. Radar images of the asteroid with size of 66 m × 32 m × 22 m under nadir observation at 900 MHz. r_g and r_a are both 1 m/pixel. (a) Radar is at position 1. (b) Radar is at position 2. The spin axis of (a) and (b) is *A*. (c) Radar is at position 1. (d) Radar is at position 2. The spin axis of (c) and (d) is *C*.

Fig. 4(a)–(d) presents the simulated radar image of the asteroid with the size 59 m × 28 m × 28 m. The range resolution and azimuth resolution are both 1 m/pixel. In Fig. 4(a) and (b), the spin axis is the longest *A*-axis. The radar observes the asteroid at positions 1 and 2 in Fig. 2(b). The nadir point has the strongest backscattering in Fig. 4(a). When the range direction is about 15 m in Fig. 4(a), the backscattering is low because the incidence angle becomes large. The other side of the ellipsoid is shaded. As a result, the simulated radar image is a semicircle in Fig. 4(a) and (b). The scattering from two sides of the imaging plane in Fig. 1 will overlap in the radar image because the range and azimuth distances are the same [11], [12]. Two sides of the asteroid are difficult to be distinguished. Because of the coherent summation of random scattering fields around each pixel, there is speckle noise in the simulated images in Fig. 4, which is also found in the Earth-based radar image of asteroids [11], [12].

Fig. 4(c) and (d) shows the radar image observed from positions 1 and 2 in Fig. 2(a). The spin axis is the shortest axis *C*. In Fig. 4(c), the length of the longest *A*-axis, which is 59 m, can be observed in the azimuth direction. In Fig. 4(d), the longest axis is in range direction. Regions with large incidence angle have low backscattering at a distance of about 20 m in range in Fig. 4(d).

Figs. 5 and 6 present the radar image of asteroid with sizes of 66 m × 32 m × 22 m and 89 m × 27 m × 19 m. The spin axis is the shortest axis in Figs. 5(a) and (b), and 6(a) and (b). The spin axis is the longest axis in Figs. 5(c) and (d), and 6(c) and (d). The main difference between Figs. 5 and 6 is the shape and the size of the asteroid in radar images. The shapes of the radar images are consistent with the cross section of the ellipsoid on the illumination plane. The backscattering is strongest at the nadir point with a minimum incidence angle. The case when the spin axis is *B* is close to that of short axis *C* since the length of *B* is close to *C*. The radar images with spin axis of *B* are not presented here.

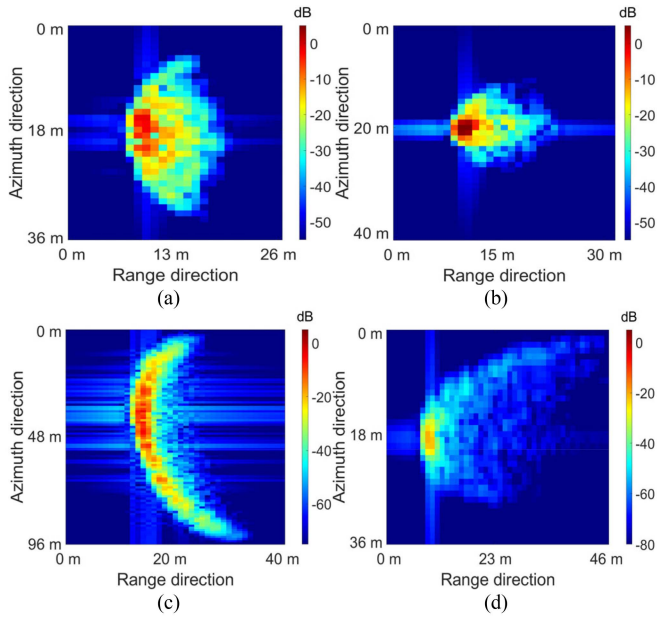

Fig. 6. Radar images of the asteroid with size of 89 m × 27 m × 19 m under nadir observation at 900 MHz. r_g and r_a are both 1 m/pixel. (a) Radar is at position 1. (b) Radar is at position 2. The spin axis of (a) and (b) is *A*. (c) Radar is at position 1. (d) Radar is at position 2. The spin axis of (c) and (d) is *C*.

B. *Oblique Observation at 900 MHz*

When the satellite is above 45°N/S, the radar observes the equator obliquely, as shown in Fig. 1. The direction of the

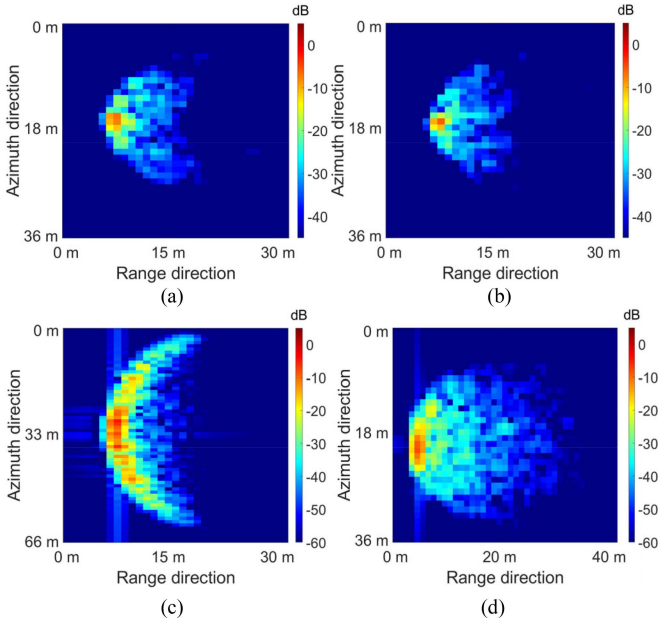

Fig. 7. Radar images of the asteroid with size of 59 m × 28 m × 28 m under oblique observation at 900 MHz. r_g and r_a are both 1 m/pixel. (a) Radar is at position 1. (b) Radar is at position 2. The spin axis of (a) and (b) is *A*. (c) Radar is at position 1. (d) Radar is at position 2. The spin axis of (c) and (d) is *C*.

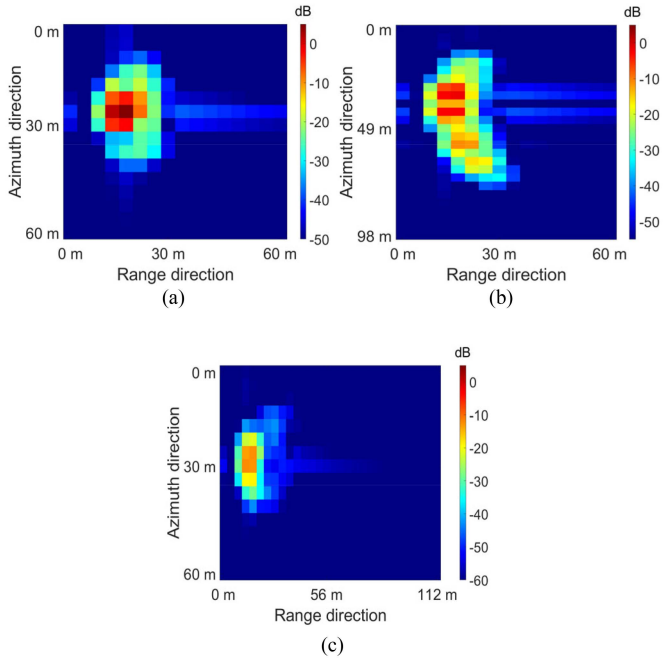

Fig. 8. Radar images of the asteroid with size of 59 m × 28 m × 28 m under nadir observation at 150 MHz. r_g and r_a are both 3.75 m/pixel. (a) Radar is at position 2. The spin axis is *A*. (b) Radar is at position 1. (c) Radar is at position 2. The spin axis of (b) and (c) is *C*.

imaging plane is different from that of nadir observation. Fig. 7 presents the radar images of the ellipsoid with size of 59 m × 28 m × 28 m under oblique observation. Half part of the ellipsoid is illuminated and the simulated radar image is semicircular. The maximum backscattering is from the nadir point. Radar images can indicate the shape of the asteroid at other latitudes under oblique observation.

C. Nadir Observations at 150 MHz

The low-frequency radar is designed to detect the internal structure with depth larger than 50 m for loss tangent of 0.01 [2]. For low-frequency radar, the scattering from internal structure should be considered. As a comparison, Fig. 8 shows the radar images of the asteroid with size of 59 m × 28 m × 28 m where the internal scatterings are not included. The resolution is 3.75 m/pixel in both azimuth and range direction. Half part of the ellipsoid is shaded and the radar images are semicircles. The strongest scattering is from the nadir point. The length of short axis is less than ten pixels. The surface scattering is likely to overlap the scatterings from internal structure at shadow layer.

Fig. 9(a)–(f) presents the radar images of the internal sphere in Fig. 3 and the radar images of the total scattering. The spin axes are *A* and *C*. The image of internal sphere can be produced by applying a 2-D inverse Fourier transform to the h_{pq}^{in} in (11). The radar image of the total scattering is produced by applying a 2-D inverse Fourier transform to the $h_{pq}^{\text{in}} + h_{pq}$ in (1) and (11). The loss tangent of medium 1 is set at 0.01 in Fig. 3 [2].

In Fig. 9(a), the spin axis is the longest axis *A* and the radar locates at position 2 in Fig. 2(b). The internal sphere locates at about 30 m in azimuth and 50 m in range direction. Fig. 9(b) presents the radar image of the total scattering. The position of the internal sphere is about 30 m away from the nadir surface point with the strongest scattering. But in the real model, the sphere is about 14 m away from the nadir surface point. The difference between the position of the sphere in radar image and the real position in physical model is caused by the propagation speed in medium 1. In (11), the speed c is $\sqrt{\varepsilon_1}$ times of the speed v in medium 1. The propagation time of the radar wave for distance of R_{in}^n in medium 1 is $\sqrt{\varepsilon_1}$ times of propagating the same distance in vacuum. In radar image in Fig. 9(b), (d), and (f), the position of internal sphere is $\sqrt{\varepsilon_1}$ times of the true position of the sphere from the nadir surface point on the ellipsoid. Here, ε_1 is 5. The distance in radar image is about 2.2 times of the real distance (14 m).

In Fig. 9(f), the azimuth position of the internal sphere is not the same as the nadir surface point (with the strongest backscattering) because the observation angle ϕ ranges from 1° to 16.28°, instead of around 0°.

The position of the internal sphere will affect the detectability. Fig. 10(a) and (b) presents the radar image of the internal sphere and the total scattering when $d = 10$ m. The center of the sphere is about 4 m away from the nadir surface point. The loss tangent is 0.01 as well. The scattering of the internal sphere is about −30 dB in Fig. 10(a). But in Fig. 10(b), it is difficult to distinguish the signal of the internal sphere from the surface scatterings. The signal of the sphere overlaps with the backscattering from asteroid surfaces. Consequently, for the internal structure that is close to the illuminated surface, the signal of the internal structure might be difficult to distinguish in radar image because of the overlapping.

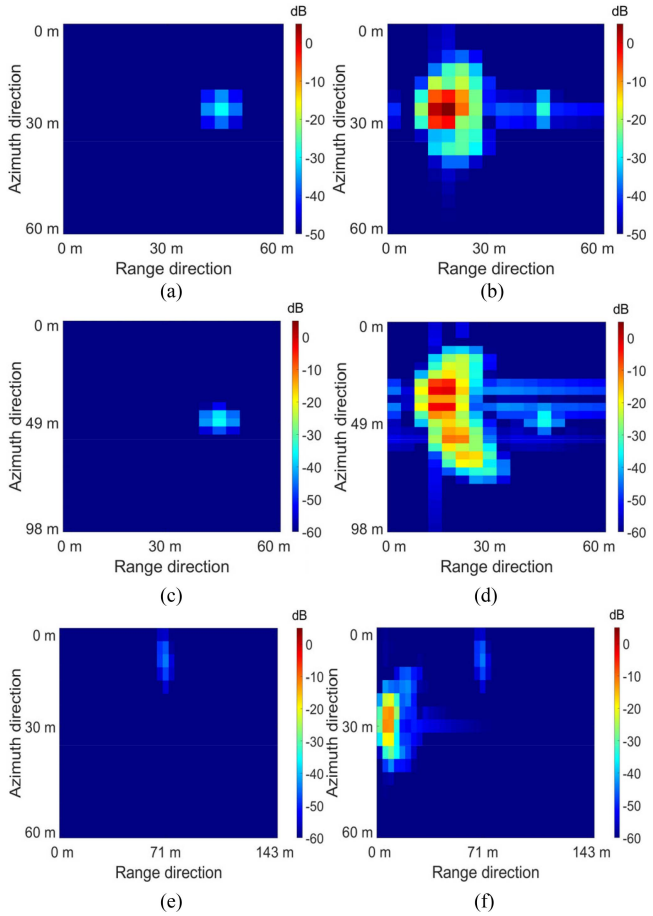

Fig. 9. Radar images of the asteroid with size of 59 m × 28 m × 28 m under nadir observation at 150 MHz. The loss tangent is 0.01 and $d = 0$ m. r_g and r_a are both 3.75 m/pixel. (a) Internal sphere. (b) Total scattering. The spin axis is A for (a) and (b) and the radar is at position 2. (c) Internal sphere. (d) Total scattering. The spin axis is C for (c) and (d) and the radar is at position 1. (e) Internal sphere. (f) Total scattering. The spin axis is C for (c) and (d) and the radar is at position 2.

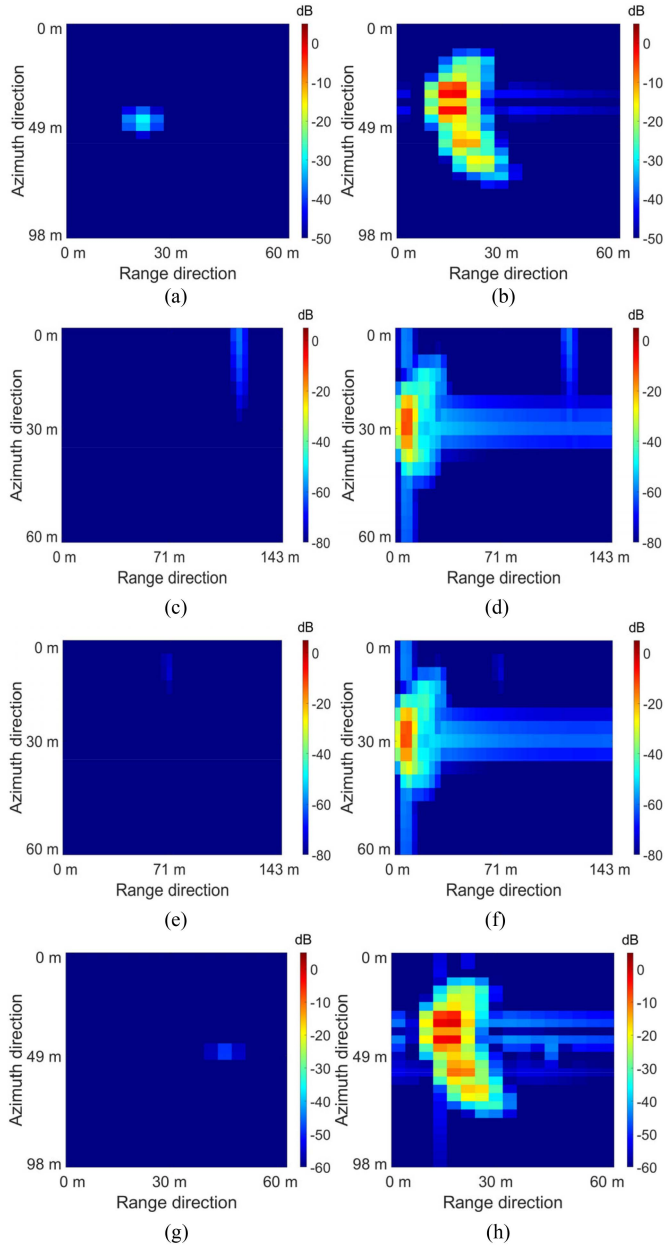

Fig. 10. Radar images of the asteroid with size of 59 m × 28 m × 28 m under nadir observation at 150 MHz. r_g and r_a are both 3.75 m/pixel. (a) Internal sphere. (b) Total scattering. The spin axis is C for (a) and (b) and the radar is at position 1. The loss tangent is 0.01 and $d = 10$ m. (c) Internal sphere. (d) Total scattering. The spin axis is C for (c) and (d) and the radar is at position 2. The loss tangent is 0.01 and $d = -20$ m. (e) Internal sphere. (f) Total scattering. The spin axis is C for (e) and (f) and the radar is at position 2. The loss tangent is 0.03 and $d = 0$ m. (g) Internal sphere. (h) Total scattering. The spin axis is C for (g) and (h) and the radar is at position 1.

Fig. 10(c) and (d) present the radar image of the internal sphere and the total backscattering when $d = -20$ m. The spin axis is C and the observation position is 2 in Fig. 2(a). The center of the small sphere is about 49.5 m away from the nadir surface point. In Fig. 9(e), the center of the small sphere is about 29.5 m away from the nadir surface point. For the loss tangent of 0.01, the absorption coefficient of the amplitude is 0.035. The attenuation coefficients are −18 and −30 dB for penetration depth of 29.5 m and 49.5 m in the medium 1. The attenuation coefficient of the backscattering from the small sphere in Fig. 10(c) is lower than that in Fig. 9(e) by 12 dB when the penetration depth increases by 20 m.

The geometry model and the observation direction of Fig. 10(e) and (f) are the same as Fig. 9(e) and (f). But the loss tangent of medium 1 is set at 0.03 in Fig. 10(e) and (f), which is in the range of loss tangents of rocks. The distance between the center of the sphere and the nadir surface point is 29.5 m. The absorption coefficient of the amplitude is 0.105 and the attenuation coefficient is −54 dB when the center of the small sphere is about 29.5 m away from the nadir surface point. In Fig. 10(f), the attenuation of the backscattering from the internal sphere is lower than that of the loss tangent of 0.01 in Fig. 9(e) and (f) by 36 dB and is more difficult to distinguish. The loss tangent of 0.01 is common to see in lunar soil [13], [19]. For the rocks with low porosity and the same mineral or chemical components as regolith, the loss tangent will be larger.

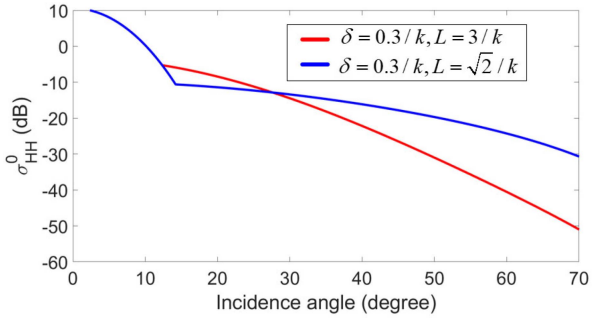

Fig. 11. Backscattering from rough surface.

In this circumstance, the detection of the internal structures at deep regions will be difficult.

The geometry model and the observation direction of Fig. 10(g) and (h) are the same as Fig. 9(c) and (d). The loss tangent is set at 0.03. The distance between the center of the sphere and the nadir surface point is 14 m. The attenuation coefficient is -26 dB. In Fig. 10(g), the attenuation coefficient from the internal sphere is larger than that in Fig. 10(e) by about 28 dB because the propagation distance is smaller. The signal of the internal sphere is easier to distinguish in Fig. 10(f). Observations from position 1 in Fig. 2(a) and positions 1 and 2 in Fig. 2(b) are more likely to distinguish the internal targets than position 2 in Fig. 2(a) because of the small propagation distance in medium 1. However, the cross bright spot will influence the detection of internal structure in Fig. 10(h). Suppression of the radar cross bright spot will be significant when processing the radar data.

When the loss tangent is 0.1, the theoretical penetration depth is 1.4 m according to (22). The absorption coefficient of the amplitude is 0.35. The attenuation coefficients are -31 and -61 dB for the penetration depths of 5 and 10 m. Radar can hardly detect internal objects when the loss tangent of the asteroid is 0.1.

IV. Discussion

A. Influence of Roughness

Because the compact polarization is composed of linear polarizations, copolarized backscattering coefficient with the small-scale surface parameters of $L_2 = 3/k$ and $\delta_2 = 0.3/k$ and $L_2 = \sqrt{2}/k$ and $\delta_2 = 0.3/k$ are presented in Fig. 11 to analyze the influence of surface roughness against the incidence angle. The small-scale roughness mainly affects the backscattering at large incidence angles. For the rough surface with small correlation $L_2 = \sqrt{2}/k$ in SPM, the backscattering at large incidence angles becomes significant in Fig. 11.

Fig. 12 presents the simulated radar image with $L_2 = \sqrt{2}/k$. The size of the asteroid is 59 m $\times$ 28 m $\times$ 28 m. The observation directions, the shape of the asteroid, and other parameters are the same as Fig. 4. Backscattering of the regions away from the nadir surface point with large incidence angle becomes larger than that in Fig. 4 because of the surface roughness. The echoes from internal embedded object are more likely to be confused by strong backscattering from rough surface.

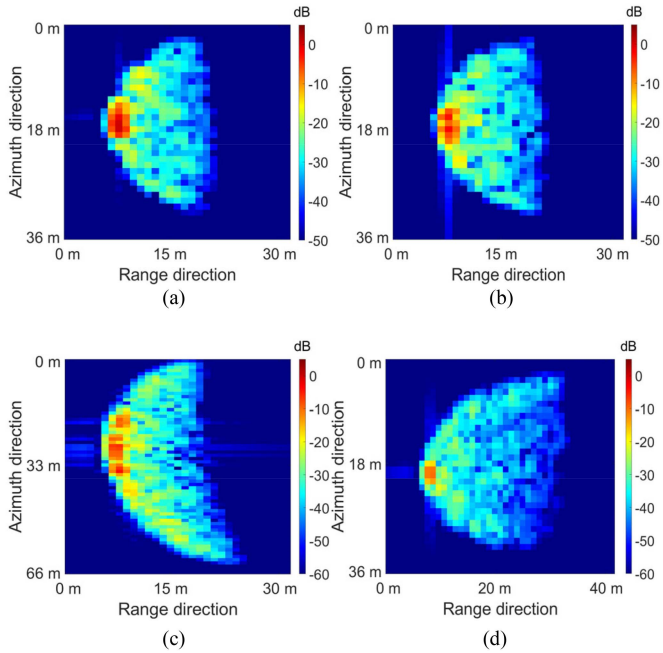

Fig. 12. Radar images of the asteroid with size of 59 m $\times$ 28 m $\times$ 28 m under nadir observation at 900 MHz. $\delta_2 = 0.3/k$ and $L_2 = \sqrt{2}/k$. r_g and r_a are both 1 m/pixel. (a) Radar is at position 1. (b) Radar is at position 2. The spin axis of (a) and (b) is A. (c) Radar is at position 1. (d) Radar is at position 2. The spin axis of (c) and (d) is C.

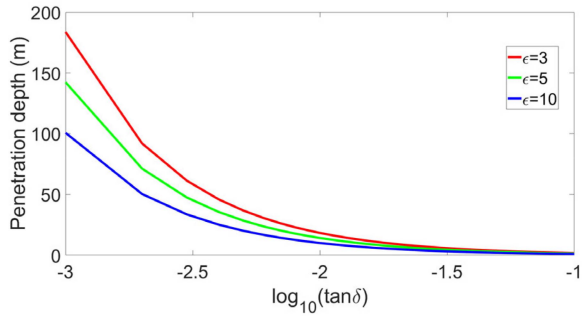

Fig. 13. Penetration depth at 150 MHz.

B. Influence of Loss Tangent

The loss tangent is one of the most significant parameters that determine the detectability of internal structures. Fig. 13 shows the penetration depth in (22) against the loss tangent at 150 MHz. The penetration depth is inversely proportional to the loss tangent and the square root of the real part of the permittivity. Increase in the ε' will decrease the penetration depth. When $\varepsilon' = 5$, the penetration depths are 142.4 m, 14.2 m, and 1.4 m for loss tangents of 0.001, 0.01, and 0.1, respectively. When $\varepsilon' = 10$, the penetration depths are 100.6 m, 10.1 m, and 1.0 m for loss tangents of 0.001, 0.01, and 0.1, respectively. The radar wave can hardly penetrate into the asteroid media when the loss tangent becomes larger than 0.1. In addition, the detectability of the echoes from the internal structure depends on its own scattering, which is influenced by the roughness, the shape, and the size of the internally embedded objects or inhomogeneous structure.

V. Conclusion

In this article, the radar images of the asteroid 2016 HO3 are simulated at 900 and 150 MHz. The two-scale model is utilized to qualitatively model the scatterings from the asteroid surface. Scatterings from asteroid surface and internally embedded sphere object are presented. It is found that the asteroid radar image at high frequency, e.g., 900 MHz, depends on the shape of the asteroid and the observation direction. The radar images of the ellipsoid are semicircles. Backscattering from this asteroid is governed by the incidence angle, surface roughness, and the dielectric constants of the object media. The radar images under oblique observation are similar to those under nadir observations. Backscattering from two sides of the imaging plane will overlay and may affect the identification of surface topography.

The influence of the loss tangent and observation directions on the detectability of internal objects inside the asteroid at 150 MHz is studied with simulations. Because the wavenumber in asteroid media is larger than that of vacuum, the distance of the internal object from the nadir surface point in radar image is larger than the real distance. If the internal object is very close to the nadir surface point, its echoes may overlay with the surface scattering and cannot be identified. With the increase in the loss tangents of the media, attenuation becomes more significant. When the loss tangent becomes larger than 0.1, the echoes from internal embedded objects can hardly be detected. The penetration depth and the surface roughness determine the detectability of internally embedded objects or internal structures. In addition, the suppression of the radar cross bright spot will be helpful for the detection of the internal structure.

In the simulation, there is no accurate large-scale and small topography in the model. Without undulation, there will be no multiple scatterings for the ellipsoid. Multiple scatterings could be considered when the data of the digital elevation model data are available. In addition, the two-scale scattering model cannot accurately describe the backscattering from rough surface. All of these factors deserve further study with advanced models when more data become available.

References

[1] C. Li et al., "Scientific objectives and payloads configuration of the Tianwen-2 mission," *J. Deep Space Exploration*, vol. 11, pp. 304–310, 2024, doi: 10.15982/j.issn.2096-9287.2024.20230185.

[2] R. Liu et al., "Design and ground experiment of asteroid internal structure detection radar (AISDR) onboard Tianwen-2 mission," in *Proc. IET Int. Radar Conf.*, Chongqing, China, 2023, pp. 3989–3993.

[3] W. Guan, Y. Su, J. Li, S. Dai, C. Ding, and Y. Liu, "Applications of ground-penetrating radar in asteroid and comet exploration," *Remote Sens.*, vol. 16, 2024, Art. no. 2188, doi: 10.3390/rs16122188.

[4] X. Li, D. J. Scheeres, D. Qiao, and Z. Liu, "Geophysical and orbital environments of asteroid 469219 2016 HO3," *Astrodynamics*, vol. 7, no. 1, pp. 31–50, 2023.

[5] J. Yan, L. Liu, M. Ye, W. Jin, D. Qiu, and J.-P. Barriot, "A simulation of the joint estimation of the GM value and the ephemeris of the asteroid 2016 HO3," *Icarus*, vol. 385, 2022, Art. no. 115120.

[6] X. Li and D. J. Scheeres, "The shape and surface environment of 2016 HO3," *Icarus*, vol. 357, 2021, Art. no. 114249.

[7] R. K. Raney et al., "The lunar mini-RF radars: Hybrid polarimetric architecture and initial results," *Proc. IEEE*, vol. 99, no. 5, pp. 808–823, May 2011.

[8] S. S. Bhiravarasu et al., "Chandrayaan-2 dual-frequency synthetic aperture radar (DFSAR): Performance characterization and initial results," *Planet. Sci. J.*, vol. 2, 2021, Art. no. 134.

[9] F. J. Meyer and D. T. Sandwell, "SAR interferometry at Venus for topography and change detection," *Planet. Space Sci.*, vol. 73, no. 1, pp. 130–144, 2012.

[10] R. M. C. Lopes et al., "Titan as revealed by the Cassini radar," *Space Sci. Rev.*, vol. 215, 2019, Art. no. 33, doi: 10.1007/s11214-019-0598-6.

[11] M. C. Nolan et al., "Shape model and surface properties of the OSIRIS-REx target asteroid (101955) bennu from radar and lightcurve observations," *Icarus*, vol. 226, pp. 629–640, 2013.

[12] M. K. Shepard et al., "Radar observations and shape model of asteroid 16 psyche," *Icarus*, vol. 281, pp. 388–403, 2017.

[13] Y. Su et al., "Hyperfine structure of regolith unveiled by Chang'E-5 lunar regolith penetrating radar," *IEEE Trans. Geosci. Remote Sens.*, vol. 60, 2022, Art. no. 5110414, doi: 10.1109/TGRS.2022.3148200.

[14] C. Liu and Y.-Q. Jin, "Radar sounder survey of seasonal and diurnal water flows on Mars surface: Simulation and SHARAD observation," *IEEE Geosci. Remote Sens. Lett.*, vol. 13, no. 12, pp. 1955–1959, Dec. 2016, doi: 10.1109/LGRS.2016.2618932.

[15] T. Kobayashi et al., "Synthetic aperture radar processing of Kaguya lunar radar sounder data for lunar subsurface imaging," *IEEE Trans. Geosci. Remote Sens.*, vol. 50, no. 6, pp. 2161–2174, Jun. 2012.

[16] C. Li et al., "Layered subsurface in Utopia Basin of Mars revealed by Zhurong rover radar," *Nature*, vol. 610, pp. 308–312, 2022.

[17] N. Liu and Y.-Q. Jin, "Simulation of pol-SAR imaging and data analysis of mini-RF observation from the lunar surface," *IEEE Trans. Geosci. Remote Sens.*, vol. 60, 2022, Art. no. 2000411, doi: 10.1109/TGRS.2021.3064091.

[18] N. Liu, F. Xu, and Y. Q. Jin, "A numerical model of CPR of rough surface with discrete scatterers for analysis of mini-RF data," *Radio Sci.*, vol. 55, no. 5, 2020, Art. no. e2018RS006776.

[19] G. H. Heiken et al., *Lunar Sourcebook: A User's Guide to the Moon*. Cambridge, U.K.: Cambridge Univ. Press, 1991.

[20] N. Liu and Y.-Q. Jin, "Pol-SAR image simulation of the lunar surface with data analysis of Chandrayaan-2 and mini-RF," *IEEE J. Sel. Topics Appl. Earth Observ. Remote Sens.*, vol. 16, pp. 10301–10310, 2023, doi: 10.1109/JSTARS.2023.3328063.

[21] F. T. Ulaby and D. G. Long, *Microwave Radar and Radiometric Remote Sensing*. Ann Arbor, MI, USA: Univ. of Michigan Press, 2014.

[22] F. T. Ulaby, R. K. Moore, and A. K. Fung, *Radar Remote Sensing and Surface Scattering and Emission Theory. Microwave Remote Sensing Active and Passive II*. Norwood, MA, USA: Artech House, 1982.

[23] Y.-Q. Jin and F. Xu, *Polarimetric Scattering and SAR Information Retrieval*. Hoboken, NJ, USA: Wiley, 2013.

[24] G. Di Martino, A. Iodice, D. Poreh, and D. Riccio, "Pol-SARAS: A fully polarimetric SAR raw signal simulator for extended soil surfaces," *IEEE Trans. Geosci. Remote Sens.*, vol. 56, no. 4, pp. 2233–2247, Apr. 2018.

[25] R. Bhalla and H. Ling, "Image domain ray tube integration formula for the shooting and bouncing ray technique," *Radio Sci.*, vol. 30, no. 5, pp. 1435–1446, 1995.

Niutao Liu (Member, IEEE) was born in Jiangsu, China, in 1994. He received the B.S. degree in telecommunication engineering from the Nanjing University of Posts and Telecommunications, Nanjing, China, in 2016, and the Ph.D. degree in electromagnetic field and microwave technology from Fudan University, Shanghai, China, in 2021.

He is currently an Associate Professor with the Key Laboratory for Information Science of Electromagnetic Waves (MoE), Fudan University. His research interests include microwave planetary remote sensing, infrared remote sensing, computational electromagnetics, and synthetic aperture radar data analysis.

Ya-Qiu Jin (Life Fellow, IEEE) B.S. degree in telecommunication engineering in atmospheric physics from Peking University, Beijing, China, in 1970, and received the M.S., E.E., and Ph.D. degrees in electrical engineering and computer science from the Massachusetts Institute of Technology, Cambridge, MA, USA, in 1982, 1983, and 1985, respectively.

He was a Research Scientist with Atmospheric Environmental Research, Inc., Cambridge, in 1985, a Research Associate Fellow of the City University of New York, in 1986 and 1987, and a Visiting Professor with the University of York, U.K., in 1993, sponsored by the U.K. Royal Society. He was also awarded the Senior Research Associateship in NOAA/NESDIS by the USA National Research Council in 1996. He is currently the Te-Pin Professor and the Director of the Key Laboratory for Information Science of Electromagnetic Waves (MoE), and Institute of EM Big Data and Intelligence Remote Sensing, Fudan University, Shanghai, China. His main research interests include electromagnetic scattering and radiative transfer in complex natural media, microwave satellite-borne remote sensing, as well as theoretical modeling, information retrieval, and applications in Earth terrain and planetary surfaces, and computational electromagnetics.

Dr. Jin is the Academician of the Chinese Academy of Sciences and the Fellow of the World Academy of Sciences for Advances of Developing World and International Academy of Astronautics. He was one of the first group of the IEEE GRSS Distinguished Speakers. He was the Co-Chair of TPC of IGARSS2011, Vancouver, Canada, and the Co-General Chair of IGARSS2016, Beijing, China. He was an Associate Editor for IEEE TRANSACTIONS ON GEOSCIENCE AND REMOTE SENSING from 2005 to 2012, and *IEEE Access* from 2016 to 2018, a member of IEEE GRSS AdCom, and the Chair of IEEE Fellow Evaluation of GRSS from 2009 to 2011. He is currently a member of the IEEE GRSS Major Awards Committee. He has authored or coauthored more than 900 papers in refereed journals and conference proceedings and 17 books, including *Polarimetric Scattering and SAR Information Retrieval* (Wiley and IEEE, 2013), *Theory and Approach of Information Retrievals From Electromagnetic Scattering and Remote Sensing* (Springer, 2005), and *Electromagnetic Scattering Modelling for Quantitative Remote Sensing* (World Scientific, 1994). He was a recipient of the IEEE GRSS Distinguished Achievement Award in 2015, Golden Florin Award in 2022, IEEE GRSS Education Award in 2010, the China National Science Prize in 1993 and 2011, the Shanghai Sci/Tech Gong-Cheng Award in 2015, the First-Grade MoE Science Prizes in 1992, 1996, and 2009, among many other prizes.

Feng Xu (Senior Member, IEEE) received the B.E.(Hons.) degree in information engineering from Southeast University, Nanjing, China, in 2003, and the Ph.D.(Hons.) degree in electronic engineering from Fudan University, Shanghai, China, in 2008.

From 2008 to 2010, he was a Postdoctoral Fellow with the National Oceanic and Atmospheric Administration Center for Satellite Application and Research, Camp Springs, MD, USA. From 2010 to 2013, he was a Research Scientist with Intelligent Automation, Inc., Rockville, MD, USA, and NASA Goddard Space Flight Center, Greenbelt, MD, USA. In 2012, he was selected into China's Global Experts Recruitment Program and, in 2013, subsequently returned to Fudan University, where he is a Professor with the School of Information Science and Technology and the Vice Director of the Key Laboratory for Information Science of Electromagnetic Waves (MoE). He has authored more than 40 articles in peer-reviewed journals, coauthored two books, and two patents, as well as publishing many conference papers. His research interests include electromagnetic scattering modeling, synthetic aperture radar information retrieval, and radar system development.

Dr. Xu was a recipient of the Second-Class National Nature Science Award of China in 2011 among other honors, the Early Career Award of the IEEE Geoscience and Remote Sensing Society (GRSS) in 2014, and the SUMMA Graduate Fellowship in the advanced electromagnetics area in 2007. He is the Founding Chair of the IEEE GRSS Shanghai Chapter. He serves as an Associate Editor for the *IEEE Geoscience and Remote Sensing Letters*.